

Journal of Nanophotonics

SPIDigitalLibrary.org/jnp

Three-dimensional point spread function of multilayered flat lenses and its application to extreme subwavelength resolution

Carlos J. Zapata-Rodríguez
David Pastor
Vicente Camps
María T. Caballero
Juan J. Miret

Three-dimensional point spread function of multilayered flat lenses and its application to extreme subwavelength resolution

Carlos J. Zapata-Rodríguez,^a David Pastor,^a Vicente Camps,^b
María T. Caballero,^b and Juan J. Miret^b

^aUniversidad de Valencia, Departamento de Óptica, Dr. Moliner 50,
46100 Burjassot, Spain
carlos.zapata@uv.es

^bUniversidad de Alicante, Departamento de Óptica, Farmacología y Anatomía,
P.O. Box 99, Alicante, Spain

Abstract. The three-dimensional (3D) point spread function (PSF) of multilayered flat lenses was proposed in order to characterize the diffractive behavior of these subwavelength image formers. We computed the polarization-dependent scalar 3D PSF for a wide range of slab widths and for different dissipative metamaterials. In terms similar to the Rayleigh criterion we determined unambiguously the limit of resolution featuring this type of image-forming device. We investigated the significant reduction of the limit of resolution by increasing the number of layers, which may drop nearly 1 order of magnitude. However, this super-resolving effect is obtained in detriment of reducing the depth of field. Limitations exist on the formation of 3D images. © 2011 Society of Photo-Optical Instrumentation Engineers (SPIE). [DOI: [10.1117/1.3590244](https://doi.org/10.1117/1.3590244)]

Keywords: metamaterials; imaging; superresolution.

Paper 11012SSR received Feb. 4, 2011; revised manuscript received Apr. 18, 2011; accepted for publication Apr. 18, 2011; published online May 20, 2011.

1 Introduction

The Cartesian ovoid of revolution is recognized to produce perfect imaging for a given conjugate pair of points by refraction.¹ In reflection, such surfaces are the conic sections. The case of the plane mirror has been unique until recently because no matter where the object lies, or whether it is “real” or “virtual,” its image in a plane mirror is completely free from monochromatic aberrations. Therefore a metal-coated flat surface generates virtual stigmatic images from three-dimensional (3D) objects. With the advent of negative-refraction-index (NRI) metamaterials now we may generate a real 3D perfect replica back in refraction. In this sense Vesselago showed for the first time that a NRI plane-parallel plate will focus radiation from a point source.² Only recently it was demonstrated this unique feature of imaging by a flat lens using the phenomenon of negative refraction in a photonic crystalline material.³ Importantly, Pendry pointed out that evanescent waves also contribute to the focal volume leading to the concept of flat superlenses which demonstrate subwavelength resolution.⁴

In principle, stigmatic imaging might be repeated sequentially in multilayered NRI slabs.⁵ This type of flat devices still conserve the properties of linearity and 3D shift invariance. On the basis of these two properties we formulated the image formation of thick objects by means of a convolution involving the 3D point spread function (PSF) of a single-layer superlens.⁶ It is obvious that the use of the scalar 3D PSF, which is evaluated for p - and s -polarized waves independently, may be extended to any stratified medium. This might be of convenience since

the 3D PSF demonstrates high suitability for evaluating the limit of resolution by using the Rayleigh criterion or some others alike.

In this paper we introduce the 3D PSF as a useful tool for the characterization of the limit of resolution, not only in the image plane but also in out-of-focus planes. We are especially interested in determining the limit of resolution of flat NRI multilayered superlenses in terms of the number of films and its geometrical distribution. Dissipation effects are also discussed. Another aspect to be considered on the formation of real images from extended objects is that the latter should be practically flat although it may contain volume details such as small grooves and surface defects. Moreover, when dealing with multiple localized emitters, they are not found necessarily in the same transverse plane though they should be placed in planes very close among themselves. With regard to this matter we discuss the limitations on the depth of field of stratiform image formers.

2 PSF of a Flat Superlens

In order to estimate the limit of resolution of a flat superlens it is possible to use the field distribution generated by a point object. Hakkarainen et al. calculated the PSF of the imaging system by investigating near-field imaging of a point dipole by a lossy, nanoscale metamaterial slab.⁷ Here we employ an alternative method in order to determine the impulse response. This approach consists of evaluating the PSF produced by a point source which is characterized by a delta function in the object plane. This is thoroughly discussed in Ref. 6 and we only give a brief summary.

Let us start by considering a NRI medium of width d , relative permittivity and relative permeability $\epsilon_2 = \mu_2 = -1 + i\delta$ for simplicity, where $\delta > 0$ stands for the absorption coefficient. In the numerical computations we preferably used $\delta = 0.1$ to obtain a qualitative assessment of our approach. In the surrounding medium $\epsilon_1 = \mu_1 = 1$. Now it is convenient to treat individually p -polarized waves and s -polarized waves. Based on the angular spectrum representation of the scattered field, for s -polarized waves, the field in the image space may be expressed as a 3D convolution in the form of

$$\vec{E}(\vec{R}, z) = \vec{E}_{sc}(\vec{R}, z - 2d) * h(\vec{R}, z), \quad (1)$$

where \vec{E}_{sc} is the electric field excited by the source, and $\vec{R} \perp \hat{z}$. The scalar 3D PSF

$$h(\vec{R}, z) = \frac{1}{(2\pi)^2} \int \int T(\vec{k}_\perp) \exp(i\vec{k}_\perp \vec{R}) \exp(i\beta_1 z) d\vec{k}_\perp, \quad (2)$$

is derived by means of the transmission coefficient between the object plane and the conjugate image plane placed at a distance $2d$,

$$T = \frac{t_{1,2}t_{2,1}e^{i(\beta_1+\beta_2)d}}{1 - (r_{2,1})^2e^{2i\beta_2d}}. \quad (3)$$

Airy's formula given above depends on the reflection coefficient at a single interface, which yields

$$r_{p,q} = \frac{\mu_q\beta_p - \mu_p\beta_q}{\mu_q\beta_p + \mu_p\beta_q} \quad (4)$$

for TE waves, and the transmission coefficient $t_{p,q} = 1 + r_{p,q}$. Finally the propagation constant

$$\beta_q = \sigma_q \sqrt{\epsilon_q \mu_q k_0^2 - \vec{k}_\perp^2}, \quad (5)$$

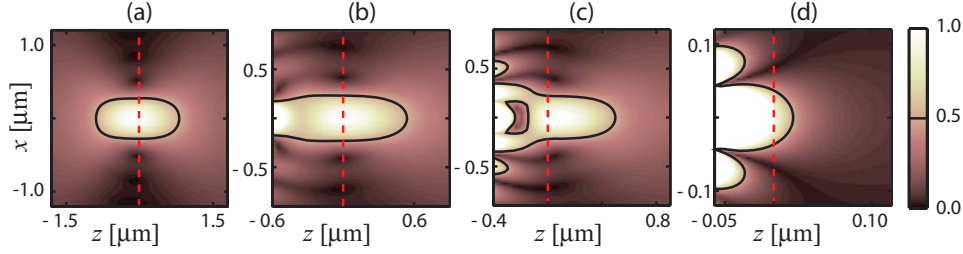


Fig. 1 Modulus of the PSF $|h|$ within $z \geq -d$ at $\lambda_0 = 600$ nm for an absorbing slab with $\delta = 0.1$ and different widths: (a) $d = 1.8 \mu\text{m}$, (b) $d = 600$ nm, (c) $d = 400$ nm, and (d) $d = 60$ nm. The density plots are normalized to unity at the geometrical focus $(x, z) = (0, 0)$. The solid line indicates points where the amplitude fall-off reaches a value $1/2$. The dashed vertical line marks the focal plane.

where $\sigma_q = 1$ for dielectrics and $\sigma_q = -1$ for NRI media, k_0 is the wavenumber in vacuum and \vec{k}_\perp is the projection of the wave vector over each flat-lens interface.

Note that $h(\vec{R}, z > 0)$ for $T = 1$, that is for $\delta = 0$, represents the propagator of the first Rayleigh–Sommerfeld integral and it is related with a divergent wave which focus is found in the image plane $z = 0$.⁸

Formally we may establish a scalar PSF for TM waves by substituting $\vec{E} \rightarrow \vec{H}$ and $\mu_q \leftrightarrow \epsilon_q$ concerning the electromagnetic fields and the constitutive parameters of the media. In general the PSFs for s - and p -polarization are different. Let us remind that $\epsilon_q = \mu_q$ is assumed not only in the surrounding medium but also in the metamaterial having negative permittivity and negative permeability. As a consequence, the transmission coefficient (3) for both polarizations are alike and therefore their corresponding PSFs are also identical. We point out that such an optimal condition might be uncommon in practice, especially concerning the term δ which represents material losses. In fact, $\epsilon_2 \neq \mu_2$ would lead to image aberrations which deserve a detailed study and therefore are not considered in this paper.

The integrand in Eq. (2) is radially symmetric so that the evaluation of the 3D PSF is simplified as

$$h(R, z) = \frac{1}{2\pi} \int_0^\infty T(k_\perp) J_0(k_\perp R) \exp(i\beta_1 z) k_\perp dk_\perp, \quad (6)$$

where the radial coordinate $R = |\vec{R}|$, and J_0 is the Bessel function of the first kind and of order 0. In Fig. 1 we represent the PSF for a moderate absorption coefficient $\delta = 0.1$ and different widths out of the interval $z \leq -d$ constituting the virtual image space. The amplitude distribution of the PSF for a slab width d below the wavelength shows a behavior different than the impulse response for $d \gg \lambda_0$. For instance, if $d = 60$ nm, the full width at half maximum (FWHM) of the PSF in the geometrical image plane yields $\Delta_\perp = 73.5$ nm, which is well below the wavelength. Moreover, the amplitude reaches a maximum value in the central point $R = 0$ over the output surface of the lens. Note that in the imaging process, the record of the subwavelength details are associated with spatial frequencies higher than k_0 which fall off fast in the transit from the output plane of the lens toward the image plane, thus frustrating a 3D focusing.⁹ On the contrary, when $d = 1.8 \mu\text{m}$ then $\Delta_\perp = 552$ nm, which is a value close to λ_0 . In this case, the amplitude maximum is found far from the output interface quite close to the image plane. Nevertheless a small axial shift of 104 nm is encountered in the direction of the lens. Finally, the FWHM along the z -axis may be evaluated in this case giving $\Delta_z = 1.70 \mu\text{m}$.

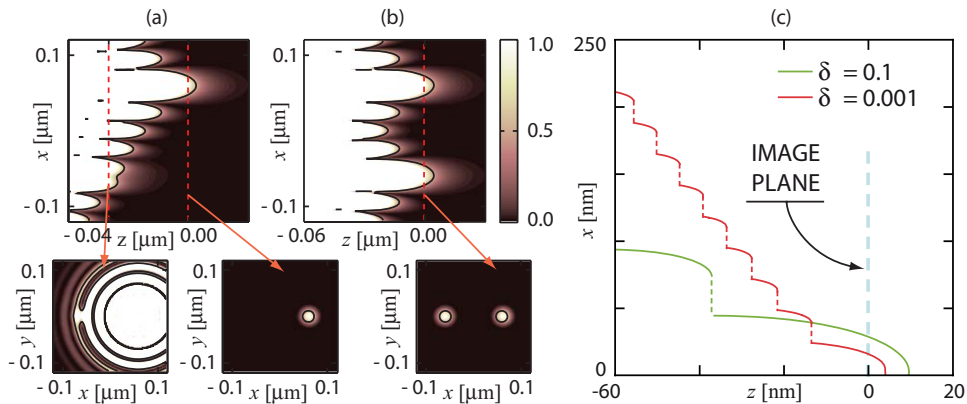


Fig. 2 Intensity in the real image space of the field excited by two incoherent point sources after passing through a superlens of $d = 60$ nm and $\delta = 0.001$. In (a) the point object O_1 is 40 nm nearer the lens than O_2 . In (b) the two sources are placed in the same transverse plane. (c) Contour of intensity $1/2$ for the 3D PSF corresponding to a point image generated by flat superlenses of different δ and placed in the xz -plane.

3 Limit of Resolution

In order to determine the limit of resolution making use of the PSF we may find diverse criteria. Perhaps the most known criterion was introduced by Lord Rayleigh,¹⁰ which establishes that two point objects are resolved if the maximum in the diffraction pattern excited by one source lies at least on the first dark ring of the diffraction pattern generated by the second source. Note that for a diffraction pattern in the form of an Airy disk, the limit of resolution coincides with 1.18 times the FWHM of the central peak in intensity. In this paper we consider a similar criterion. Specifically we simply consider the FWHM of the PSF as the limit of resolution of the image-forming system.

Figure 2 illustrates our criterion by showing the field intensity produced by two equienergetic point sources in the image space of the flat superlens analyzed in Fig. 1(d). In particular, one of the point objects O_1 is located at $\mathbf{R}'_1 = (60 \text{ nm})\hat{x}$ and the second point object O_2 is displaced to $\mathbf{R}'_2 = (-60 \text{ nm})\hat{x}$. For the evaluation of the intensity distribution we assume that the electromagnetic field is formed by the incoherent superposition of the waves emitted by both sources, putting a stop to spurious interference effects. This is fully consistent with approximations commonly employed in fluorescence microscopy.¹¹ In this case, the distribution of intensity is proportional to

$$\sum_{j=1,2} |h(\mathbf{R} - \mathbf{R}'_j, z - z'_j)|^2, \quad (7)$$

where z'_j denotes the location of the two geometrical image planes. Every graphical representation in Fig. 2 is normalized to unity at the image point O'_1 . Additionally, the contour line denotes an intensity that has fallen down to a value $1/2$.

Figure 2(a) shows that if the point object O_1 remains 40 nm nearer the superlens than O_2 , its geometrical image O'_1 is located in a plane ($z'_1 = 0$) further from the output plane of the lens. The presence of the secondary image O'_2 is practically unperceivable in this transverse plane because of the evanescent nature of the image field generated at $z'_2 = -40$ nm. Shifting to the plane of the geometrical image O'_2 , it can be caught. However the intensity distribution is superimposed with an intense back tail of the PSF produced by O'_1 . Moreover, the contour of intensity $1/2$ wrapping around the image point O'_2 in the image plane z'_2 also envelopes the diffraction pattern of O'_1 . Consequently both images are not perfectly resolved. However in Fig. 2(b) we observe that when both sources are co-planar then both images may be resolved.

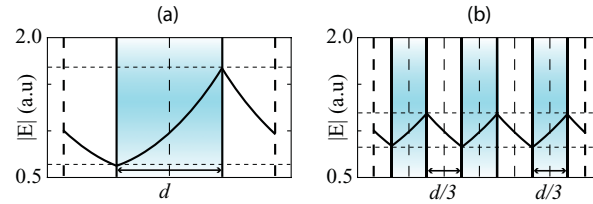


Fig. 3 Evanescent wave field with transverse spatial frequency $k_{\perp} = 2k_0$ traveling from the object plane to the image plane of a flat monolayer and a trilayer superlens. In all cases $\lambda_0 = 600$ nm, $\delta = 0.1$, and $d = 60$ nm. Thick dashed lines indicate the position of the object plane and the final image plane. Thin dashed lines denotes intermediate image planes.

In Fig. 2(c) we represent the contour of intensity 1/2 corresponding to the normalized 3D PSF for different NRI flat lenses of width $d = 60$ nm. In the numerical simulations, the wavelength $\lambda_0 = 633$ nm remains the same. In the geometrical image plane, the film of $\delta = 0.001$ shows a PSF in irradiance with a radius 12.5 nm, significantly lower than 27.3 nm attributed to a NRI superlens of $\delta = 0.1$. Such a super-resolving behavior is kept in neighbouring transverse planes. However, the contribution of the intense sidelobes leads to an increment of the limit of resolution for $\delta = 0.001$. In this particular case we observe that the first lateral peak determines the limit of resolution within the interval -21.6 nm $< z < -13.6$ nm, and the second sidelobe is determinant in planes at -27.8 nm $< z < -21.6$ nm, up to 8 sidelobes influencing the limit of resolution in the real image space. In the case $\delta = 0.1$, however, only the first sidelobe may contribute effectively.

4 Extreme Super-resolution in Multilayered Structures

Originally the flat superlens was conceived as an image-forming system composed of a single NRI slab.² Also a silver nanolayer demonstrates the ability of generating an image with sub-wavelength features.⁴ Soon it was shown that the limit of resolution of a metallic superlens might be reduced substantially if it is substituted by a set of layers with free-space in between.¹² This improvement is based on the lesser amplification of evanescent waves, so that dissipative effects also diminish. In Fig. 3 we compute the electric field of an evanescent wave field with transverse spatial frequency $k_{\perp} = 2k_0$ propagating from the object plane toward the image plane for two different superlenses: a one lens is composed of a single layer of width d and b the second lens is composed of three equidistant films of width (and separation) $d/3$. In all cases $\lambda_0 = 600$ nm, $\delta = 0.1$, and $d = 60$ nm. The amplification of the evanescent wave in the multilayered superlens is significantly lower. The existence of secondary images in the intermediate spaces allows that new evanescent waves with higher spatial frequency contributes effectively in the formation of the final image, thus improving the resolution power.⁵ This idea is being upgraded in recent years.^{13–16}

A general NRI multilayer flat lens is sketched in Fig. 4. Inside the lensing arrangement N NRI layers are distributed uniformly. Every thin film has a width d/N . Therefore d denotes the resultant length after summing up the widths of all the layers, leading to a distance $2d$ between the plane of the object and the final geometrical image plane. Note that every interface dielectric-NRI generates a stigmatic image that acts as an object for the next interface, giving $2N - 1$ secondary images. The distance between two adjacent layers is fd/N , where f is a non-dimensional coefficient of proportionality. The width of the multilayer arrangement e results by summing up N NRI films and $N - 1$ interspaces,

$$e = d \left(1 + f \frac{N - 1}{N} \right). \quad (8)$$

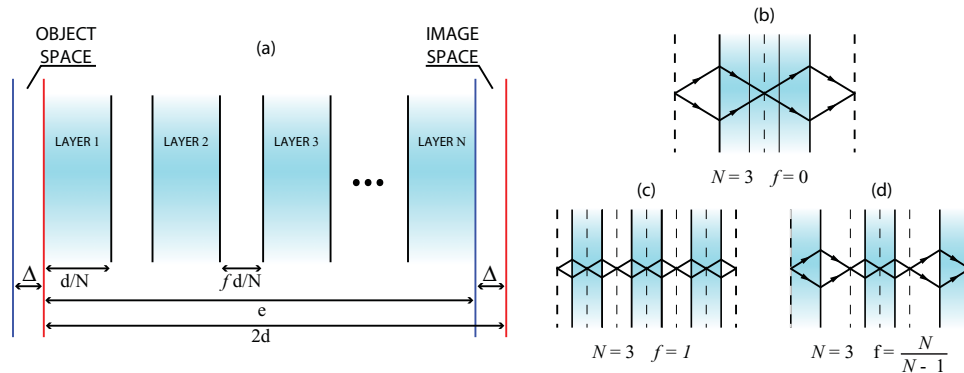


Fig. 4 (a) Scheme of a multilayered superlens containing N uniformly-distributed films. We indicate the zones where we may encounter real conjugated pairs simultaneously. The parameter Δ denotes the width of these two zones. On the right we represent different trilateral superlenses. From (b) to (d), the distance between NRI films increases gradually. Object and final image planes are represented by thick dashed lines, and secondary images are denoted by thin dashed lines.

In order to generate a real image, the superlens width e should be lower or at least the same as the distance between the object plane and the image plane, $e \leq 2d$. In this case f ranges within the interval

$$0 \leq f \leq \frac{N}{N-1} \leq 2, \quad (9)$$

and the natural number $N \geq 2$.

Let us point out three cases of special interest. First, if $f = 0$ the set of N films are stacked so that the optical system behaves like a monolayer superlens of width d as shown in Fig. 4(b). When $f = 1$ the NRI films and the free space in between coincide in breadth, as illustrated in Fig. 4(c). Finally in the limit $f = N/(N - 1)$, the input and output faces of the arrangement are in contact with the object and image planes, respectively. This is depicted in Fig. 4(d).

In order to evaluate the limit of resolution corresponding to multilayer superlenses we estimate the FWHM of the 3D PSF once again. In this case the transmission coefficient T used in Eq. (2) is computed by using the characteristic matrix formulation for isotropic stratified media.¹⁷ In the numerical simulations we use a NRI material of total width $d = 60$ nm and with an absorption coefficient $\delta = 0.1$; also the radiation wavelength is $\lambda_0 = 632.8$ nm. The results are shown in Fig. 5(a). Within the interval $0 \leq f \leq 1$ the FWHM exhibits a linear decreasing behavior. However its value is maintained constant for $f > 1$. On the other hand, the FWHM decreases if the number N of layers increases up to a saturation limit. In practical terms we may consider that 128 layers represents this limiting case, for which the FWHM is only 8.82 nm.

The multilayer superlens turns up as an alternative of special interest in comparison with the monolayer case since the former reduces the limit of resolution significantly. However this sort of device withstands a major difficulty in order to generate real images. In the first place,

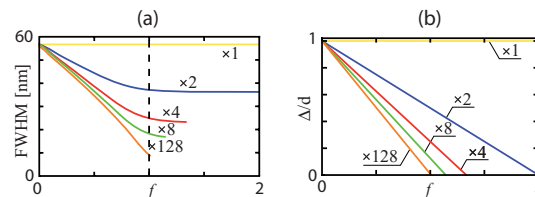


Fig. 5 (a) Limit of resolution for flat superlenses of different number N of layers and separation f , keeping $d = 60$ nm fixed. (b) Depth of field normalized to d as a function of f .

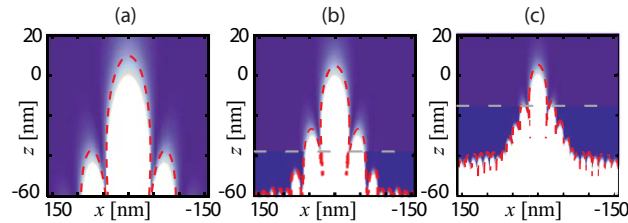


Fig. 6 Intensity of the PSF in the plane xz of the image volume for a superlens of $N = 4$ layers and: (a) $f = 0$, (b) $f = 1/2$, and (c) $f = 1$. The dashed line represents the boundary of the real image space.

the scattering objects should be located closer to the entrance face of the superlens, and as a consequence the conjugate images are also found nearer the output interface. For convenience we introduce the definition of the depth of field Δ as the width of the two zones where we may encounter real conjugate pairs of objects and images, simultaneously. Such a width is obtained by considering the distance object-image and subtracting the superlens width, $\Delta = 2d - e$. By utilizing (8), we finally obtain

$$\Delta = d \left(1 - f \frac{N-1}{N} \right). \quad (10)$$

Equation (10) provides a linear relationship between the depth of field and the distance from adjacent layers. Note that Δ is reduced if the interspace width increases.

The depth of field (10) as a function of f is depicted in Fig. 5(b) for different number N of layers. It is shown that increasing the interspace between layers reduces the depth of field linearly. The slope of these straight lines, $(1 - N)/N$, quickly drops when the number N of layers increases, reaching the limiting value -1 .

By comparing Figs. 5(a) and 5(b) we conclude that an increase in the number N of layers leads to a reduction of the limit of resolution. This effect is achieved in detriment of reducing the depth of field, which results highly harmful in the formation of 3D images. This tendency is repeated if the interspace between layers increases. Optimization of the geometrical coefficient f might consist of reaching a trade-off between the limit of resolution and the depth of field necessary for a specific application.

We have computed the 3D PSF for $N = 4$ nanolayers and different values of f , which are depicted in Fig. 6. In the numerical simulation, the wavelength is set $\lambda_0 = 632.8$ nm, and the parameters characterizing the NRI medium are $d = 60$ nm and $\delta = 0.1$. In Fig. 6 we observe that a higher f goes with a narrower central peak of the 3D PSF, involving a resolution improvement in transverse planes close to focus, $z = 0$, where sidelobes may be neglected. However evanescent tails grow up with f , which are plainly seen in planes near the focal plane. These sidelong peaks lead to discontinuities in the limit of resolution, which are derived from our criterion of resolution, likewise the case $N = 1$ previously analyzed. In particular, the first discontinuity is found at $z = -37.7$ nm in Fig. 6(a) and it is shifted to $z = -14.5$ nm in Fig. 6(c). We remind that a higher interspace between layers, that is an increment of f , forces a deterioration of the depth of field. In this sense we have included a dashed line in each subfigure to mark the boundary $z = -\Delta$ delimiting the real image space and the virtual image space. It is confirmed that an increase of f leads to a depth-of-field falloff.

5 Conclusions

Finally we conclude that layered metamaterial superlenses show an improved resolution power in comparison with image-forming monolayer devices. However this negatively affects the depth of field and the ability of observing images out of the geometrical image plane. Therefore,

the design of a multilayer superlens involves a trade off between a required resolution power and the limitations it includes in the process of recording an image in volume.

The 3D PSF analysis presents potential applications for the complete and simple description of the image formation in stratified metamaterials and one-dimensional photonic crystals. This model is also appropriate for flat-lens designs using metal-dielectric multilayered structures.

Acknowledgments

This research was funded by Ministerio de Ciencia e Innovación (MICIIN) under the project TEC2009-11635.

References

1. F. L. Pedrotti and L. S. Pedrotti, *Introduction to Optics*, Prentice-Hall, Englewood Cliffs, NJ (1993).
2. V. G. Veselago, "The electrodynamic of substances with simultaneously negative values of ϵ and μ ," *Physics-Uspekhi* **10**(4), 509–514 (1968).
3. P. V. Parimi, W. T. Lu, P. Vodo, and S. Sridhar, "Imaging by flat lens using negative refraction," *Nature (London)* **426**, 404 (2003).
4. J. B. Pendry, "Negative refraction makes a perfect lens," *Phys. Rev. Lett.* **85**, 3966–3969 (2000).
5. S. A. Ramakrishna, J. B. Pendry, M. C. K. Wiltshire, and W. J. Stewart, "Imaging the near field," *J. Mod. Opt.* **50**, 1419–1430 (2003).
6. C. J. Zapata-Rodríguez, D. Pastor, and J. J. Miret, "Three-dimensional point spread function and generalized amplitude transfer function of near-field flat lenses," *Appl. Opt.* **49**, 5870–5877 (2010).
7. T. Hakkarainen, T. Setälä, and A. T. Friberg, "Subwavelength electromagnetic near-field imaging of point dipole with metamaterial nanoslab," *J. Opt. Soc. Am. A* **26**, 2226–2234 (2009).
8. M. Nieto-Vesperinas, "Problem of image superresolution with a negative-refractive-index slab," *J. Opt. Soc. Am. A* **21**, 491–498 (2004).
9. R. Marques, M. J. Freire, and J. D. Baena, "Theory of three-dimensional subdiffraction imaging," *Appl. Phys. Lett.* **89**, 211113 (2006).
10. M. Born and E. Wolf, *Principles of Optics*, 7th (expanded) ed., Cambridge University Press, Cambridge, UK (1999).
11. C. Girard and A. Dereux, "Near-field optics theories," *Rep. Prog. Phys.* **59**, 657–699 (1996).
12. E. Shamonina, V. A. Kalinin, K. H. Ringhofer, and L. Solymar, "Imaging, compression and Poynting vector streamlines with negative permittivity materials," *Electron. Lett.* **37**, 1243–1244 (2001).
13. Z. Jaksic and M. Maksimovic, "Ordered artificial nanocomposites for imaging beyond diffraction limit," in *Proc. 1st International Workshop on Nanoscience & Nanotechnology IWON 2005*, pp. 147–156, Belgrade (2005).
14. B. Wood, J. B. Pendry, and D. P. Tsai, "Directed subwavelength imaging using a layered metal-dielectric system," *Phys. Rev. B* **74**, 115116 (2006).
15. D. de Ceglia, M. A. Vincenti, M. G. Cappeddu, M. Centini, N. Akozbek, A. D'Orazio, J. W. Haus, M. J. Bloemer, and M. Scalora, "Tailoring metallodielectric structures for superresolution and superguiding applications in the visible and near-IR ranges," *Phys. Rev. A* **77**, 033848 (2008).
16. R. Kotyński and T. Stefaniuk, "Multiscale analysis of subwavelength imaging with metal dielectric multilayers," *Opt. Lett.* **35**(8), 1133–1135 (2010).
17. P. Yeh, *Optical Waves in Layered Media*, Wiley, New York (1988).

Biographies and photographs of the authors not available.